Repositorio Institucional de la Universidad Autónoma de Madrid

https://repositorio.uam.es

Esta es la **versión de autor** del artículo publicado en:
This is an **author produced version** of a paper published in:

Biological Psychology 118 (2016): 114-125

DOI: http://dx.doi.org/10.1016/j.biopsycho.2016.05.009

Copyright: © 2016 Elsevier B.V. All rights reserved

El acceso a la versión del editor puede requerir la suscripción del recurso
Access to the published version may require subscription

Retinotopic Mapping of Visual Event-Related Potentials

Almudena Capilla[1], María Melcón[1], Dominique Kessel[1], Rosbén Calderón[1], Paula Pazo-Álvarez[2], Luis Carretié[1]

[1] Departamento de Psicología Biológica y de la Salud, Facultad de Psicología, Universidad Autónoma de Madrid, Madrid, Spain

[2] Departamento de Psicoloxía Clínica e Psicobioloxía, Facultade de Psicoloxía, Universidade de Santiago de Compostela, Santiago de Compostela, Spain

CORRESPONDING AUTHOR: Almudena Capilla, PhD, Facultad de Psicología, Universidad Autónoma de Madrid, C/ Ivan Pavlov 6, 28049, Madrid, Spain. E-mail: almudena.capilla@uam.es. Tel: +34 91 497 3383.

KEYWORDS: Beamforming; Event-Related Potential (ERP); Independent Component Analyses (ICA); Pattern-reversal; Retinotopic mapping; Source localization; Visual cortex; Visual Evoked Potential (VEP).

ABSTRACT

Visual stimulation is frequently employed in electroencephalographic (EEG) research. However, despite its widespread use, no studies have thoroughly evaluated how the morphology of the visual event-related potentials (ERPs) varies according to the spatial location of stimuli. Hence, the purpose of this study was to perform a detailed retinotopic mapping of visual ERPs. We recorded EEG activity while participants were visually stimulated with 60 pattern-reversing checkerboards placed at different polar angles and eccentricities. Our results show five pattern-reversal ERP components. C1 and C2 components inverted polarity between the upper and lower hemifields. P1 and N1 showed higher amplitudes and shorter latencies to stimuli located in the contralateral lower quadrant. In contrast, P2 amplitude was enhanced and its latency was reduced by stimuli presented in the periphery of the upper hemifield. The retinotopic maps presented here could serve as a guide for selecting optimal visuo-spatial locations in future ERP studies.

HIGHLIGHTS

- Extensive and multichannel retinotopic mapping of major visual ERP components.
- C1 and C2 components showed inverted polarity for upper and lower hemifields.
- P1 and N1 components were larger when the contralateral lower field was stimulated.
- P2 showed higher amplitude and shorter latency for peripheral upper field stimuli.
- Present results can be used to select optimal stimulus locations in ERP designs.

INTRODUCTION

Electroencephalographic (EEG) research makes frequent use of visual stimulation to study a variety of cognitive processes, such as perception, attention or memory. Typically, the EEG activity time-locked to stimulus onset is averaged, resulting in the so-called visual event-related potentials (ERPs; also known as visual evoked potentials, VEPs). Visual ERPs can be quantified in terms of the amplitude, latency and topography of their constituent components (Key et al., 2005). Critically, these components are affected not only by the visual stimulus features or experimental manipulation but also by the spatial location of stimulation. The reason for this is that scalp EEG activity largely depends on the geometry of the underlying brain sources (Nunez, 1981; Nunez and Srinivasan, 2006), and in the case of the visual cortex these are retinotopically organized (Sereno et al., 1995; Wandell et al., 2007). A prime example is C1, the first visual ERP component, which reverses in scalp polarity as stimuli are presented in either the upper or the lower visual field (Di Russo et al., 2002; Martinez et al., 1999). This is due to the opposite orientation of the neurons coding upper and lower hemifields in the primary visual cortex (V1), the putative neural generator of C1 as postulated by the "cruciform model" (Jeffreys and Axford, 1972a, 1972b).

The interest in the retinotopic variations of the visual ERPs has been almost exclusively focused on the C1 component (Ales et al., 2010b, 2013; Clark et al., 1995; Kelly et al., 2013a, 2013b). However, we still lack a detailed retinotopic map of later components, which are more commonly studied in the ERP literature, such as P1 and N1 (Di Russo et al., 2012; Klimesch, 2011; Mangun et al., 1998). For instance, it has recently been demonstrated that the amplitude of some components such as P1 or the face-sensitive

N170 is modulated by the gaze fixation position within a face (Zerouali et al., 2013). A systematic description of how visual ERP components differ as a function of stimulus location might assist not only in the interpretation of research findings but also in the design of ERP experiments, for example, by optimizing stimulus position to study a given component.

To our knowledge, only two lines of research have partially addressed this issue. The first one refers to studies employing the multifocal visual evoked potential technique (mfVEP), mainly developed for clinical neuro-ophthalmological purposes (e.g. to improve the diagnosis of patients with glaucoma or optic neuritis/multiple sclerosis; Baseler and Sutter, 1997; Baseler et al., 1994; Fortune and Hood, 2003; Hood et al., 2003; Sutter, 2001; Zhang and Hood, 2004; but see also Bach, 2006). This technique consists in the rapid stimulation of different sectors of the visual field with very good coverage (close to 45° of visual angle). However, the extremely short SOAs (stimulus onset asynchrony, ~17 ms for a monitor refresh rate of 60 Hz) generate strong adaptation effects on visual ERP components, especially on those with extrastriate generators (Fortune and Hood, 2003). Furthermore, these studies have usually recorded brain activity using a limited array of 1-3 electrodes (Oz and/or POz/O1/O2). The second line of research has employed stimulation and recording protocols typically used in ERP studies (e.g. SOAs > 200 ms and multichannel scalp recordings; Clark et al., 1995; Di Russo et al., 2002, 2005). However, these studies have not exhaustively covered the visual field. Instead, they have used stimulation at isoeccentric positions restricted to perifoveal regions (e.g. 4°-8° eccentricity).

Thus, our study aimed to provide a detailed guide on how the spatial location of visual stimuli influences ERP components. To this end, we carried out a systematic retinotopic

mapping of amplitude and latency variations of visual ERPs, combining the best of both previous approaches. As in mfVEP studies, we stimulated the visual field from the fovea to the periphery (up to 22° eccentricity radius) at different polar angles (in 30°-45° steps). However, in line with previous ERP studies (Clark et al., 1995; Di Russo et al., 2002, 2005), we employed multichannel EEG recordings and larger SOAs (200-400 ms) with a twofold aim: to reduce neural adaptation and to strengthen the contribution of extrastriate cortex. In addition, we used beamforming analysis (Gross et al., 2001; Van Veen et al., 1997) to localize the neural origin of the visual ERP components.

MATERIALS AND METHODS

Participants

Thirty-two healthy volunteers participated in the study. However, as explained later, only data from 29 of them were analyzed (13 males; 27 right-handed; mean ± SD age: 22.8 ± 2.0). All participants reported normal or corrected-to-normal vision. They all provided informed written consent before their participation. The study was approved by the Universidad Autónoma de Madrid's Ethics Committee and conducted in conformity with the declaration of Helsinki.

Stimuli and Procedure

The experiment was conducted inside an electrically shielded, sound-attenuated room. Stimuli were presented on a back-projection screen through a RGB projector, while participants seated in a comfortable chair at 50 cm from the screen.

Stimuli consisted of a dartboard centered on a gray background, as employed in mfVEPs studies (Baseler et al., 1994; Horton and Hoyt, 1991b; Wu et al., 2012). The diameter of the dartboard was 40 cm. It was divided into 60 sectors of different polar angle and eccentricity. Each sector comprised a white and black checkerboard of 4 by 4 checks, scaled accordingly to compensate for cortical magnification (Baseler et al., 1994; Horton and Hoyt, 1991b; Wu et al., 2012). Thus, the sectors were placed in six concentric rings of radius 1.2°, 2.6°, 5.8°, 9.8°, 14.9° and 22.2° (see Figure 1).

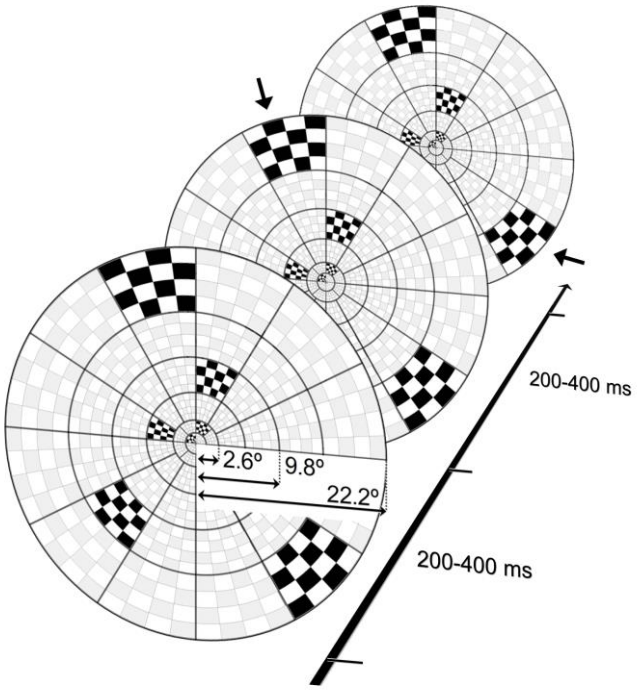

Figure 1. Stimulation design. Dartboard composed of 60 scaled sectors of different polar angle and eccentricity. Each sector contained a 4 by 4 checkerboard stimulus (for visualization purposes, only a selection of them is shown in black and white, and the rest are shaded). In each trial the checks at a pseudo-randomly selected sector reversed polarity, while the rest of them remained stationary. The figure shows three example trials. Note the pattern reversals (indicated by arrows) at a sector located at the peripheral upper left quadrant in the second trial, and at the peripheral lower right quadrant in the last trial. Stimulus onset asynchrony (SOA) varied randomly between 200 and 400 ms.

Visual stimulation was carried out using Psychtoolbox (v3.0; Brainard, 1997). Trials consisted of one contrast reversing check pattern (i.e. in each trial the black checks of a given sector turned white, and the white checks turned black). The checkerboard did not return to its original phase, but instead continued with the same black-white configuration until this sector was stimulated later again (see Figure 1). These single pattern reversals at each sector were pseudo-randomly sequenced with the restrictions that a given sector was never repeated in two consecutive trials, and each one reversed a total of 80 times across the whole experiment. The stimulus onset asynchrony (SOA) between pattern reversals presented at different sectors varied randomly between 200 and 400 ms. This timing aimed to reduce adaptation effects, compared to the < 20 ms SOA typically employed in mfVEP studies (Fortune and Hood, 2003; Hood et al., 2003), and it has been shown to effectively prevent overlap between successive responses (Capilla et al., 2011). ERP overlapping was further prevented by stimulating different sectors of the visual field in consecutive trials, as previously mentioned.

This resulted in a total number of 4800 trials (80 pattern reversals x 60 sectors) that were organized in 8 blocks. Each block consisted of 12 series of 50 trials (600 trials), each series lasting around 15 seconds, with 2 seconds breaks between them. During the breaks, the screen turned gray and participants were invited to blink and rest their eyes. In addition, participants were allowed short, self-paced breaks between blocks. At the beginning of each series, the dartboard was presented over the gray background. It remained stationary for 2 s before the first checkerboard was reversed. The experiment lasted between 30 and 35 minutes including breaks; thus, each block lasted less than 4 minutes.

A blue fixation point indicated the center of the dartboard. Participants were given verbal instructions to maintain their gaze on the central fixation point throughout the whole experiment. To facilitate that participants maintained fixation, a secondary task (Clark et al., 1995; Di Russo et al., 2002) consisting in the detection of a brief color change was included (i.e. in 5% of the trials, the blue point turned red for 100 ms). Participants were asked to count and report the number of color changes at the end of each series. Trials containing a color change were discarded from subsequent analysis.

Recording of the EEG Signal

EEG activity was recorded using an electrode cap with tin electrodes (custom-made by ElectroCap International) and a Contact Precision Instruments system (http://psychlab.com). Fifty-nine electrodes were placed at the scalp according to the International 10-10 System. They all were referenced to the nose-tip and grounded with an electrode attached on the forehead. Electrical activity elicited by vertical and horizontal eye movements was monitored by electrooculogram (EOG) recorded bipolarly from above and below the right eye and on the outer canthi of both eyes. Recordings were continuously digitized at a sampling rate of 420 Hz and filtered on-line with an analog bandpass of 0.3-1000 Hz.

Analysis of the EEG Signal

EEG data analysis was performed using the Fieldtrip toolbox (Oostenveld et al., 2011; http://fieldtrip.fcdonders.nl) and in-house Matlab code (The MathWorks). Overall, the analysis of the EEG signal aimed to characterize modulations of ERP components by stimulation through the visual field. To achieve this aim, we first preprocessed the data and removed artifactual activity.

Then, a three step analysis at the electrode- or sensor-level was carried out. First, ERP waveforms and topographies for different stimulus locations were computed. The rationale for this step was to provide a general description of the influence of stimulus location on visual ERPs. The advantage of this preliminary analysis is that the obtained results can be directly comparable between studies. However, as it will be shown later, the main ERP components showed some degree of overlap, making difficult the quantification of ERP components features, specially their amplitude. In order to overcome this problem, a second analysis step employed independent component analysis (ICA) to obtain a set of ICs that captured the ERP components of interest. In the third analysis step, and in accordance with the main aim of the study, the retinotopic distributions of amplitude and latency for each IC ERP component were obtained.

Finally, we extended our analysis to the source-level. The aim of this analysis was to estimate the brain sources underlying the previously identified ERP components, in order to increase our understanding of the retinotopic variations observed at the sensor-level. To this end, we combined beamforming and ICA (see Capilla et al., 2013), using an analogous approach to the previous one applied at the sensor-level.

These steps are explained in detail in the following subsections.

Preprocessing

The EEG signal was digitally low-pass filtered below 30 Hz. Then, the continuous EEG signal was epoched into segments of 500 ms (-100 ms to 400 ms relative to each pattern reversal onset), baseline corrected, and assigned to one out of 60 conditions depending on the sector where visual stimulation took place. Epochs containing blinks or eye-

movements exceeding ±50 μV were automatically discarded from further analyses (Verleger, 1993). Also, trials with other stereotyped and non-stereotyped artifacts (e.g. cable movement, swallowing, muscular artifacts, etc.) were visually inspected and manually removed. Artifact rejection resulted in an average of 67.4 ± 6.5 (mean ± SD) epochs per participant and condition. One-factor repeated-measures ANOVAs performed on artifact-free mean number of trials did not reveal differences among sectors ($F_{59,1652}$ = 0.9, p > 0.5). Finally, electrodes showing artifactual activity throughout the recording were linearly interpolated based on the activity of neighboring electrodes (mean ± SD of interpolated electrodes 2.1 ± 2.4). Data from two participants showing an excessive number of noisy electrodes (more than 20% of the total number of electrodes) were discarded from the analyses.

Sensor-Level ERPs and Topographies

First, preliminary analyses were performed in order to provide a general description of the main ERP components in terms of amplitude, latency and topography, and how these features changed as a function of polar angle and eccentricity. Thus, artifact-free epochs were selectively averaged for each sector. For visualization purposes, they were also merged in 12 (see Figure 2) and 16 (Figures 3 and 4) sections of visual field. These sections were grouped based on their polar angle (right/left, upper/lower quadrants) and eccentricity (foveal, perifoveal and peripheral rings; radius < 2.6°, 2.6° to 9.8°, and 9.8° to 22.2°, respectively).

Independent Component Analysis (ICA) of Sensor-Level ERPs

One method for dealing with the problem of spatiotemporally overlapping ERP components is ICA (Makeig et al., 1996). In order to obtain a more precise

characterization of the visual ERPs, extended infomax ICA (Bell and Sejnowski, 1995; Lee et al., 1999) was applied on the previously computed sensor-level ERPs for each sector and participant (60 x 29 ERPs for each electrode) ('runica' EEGLAB algorithm implemented in FieldTrip; http://sccn.ucsd.edu/eeglab/).

Meaningful independent components (ICs) were selected by visual inspection, comparing their scalp topographies and time courses with the previously identified ERP components. Then, the percent variance accounted for by each of them was computed. IC activation magnitudes were normalized by multiplying each by the root-mean square (RMS) amplitude of the corresponding IC scalp map. This normalization was performed to convert the unit of IC waveforms from arbitrary (a.u.) back to the original recorded unit (microvolt) (Onton and Makeig, 2006). In addition, as the polarity returned by ICA is also arbitrary, IC waveforms were multiplied by either a positive or a negative sign to match the polarity observed at the scalp (e.g. a positive polarity for P1). Finally, as in previous analyses, averages for each sector as well as for groups of sectors were computed for visualization purposes (see Figure 5).

Retinotopic Distribution of each ERP Component's Amplitude and Latency

This analysis was aimed at characterizing the retinotopic variations in amplitude and latency of the previously identified IC-ERP components. Thus, for each of the selected IC and visual field sector, the amplitude and peak latency of selected IC-ERP components were manually extracted. This information was plotted as a function of the stimulated sector position to obtain the measured retinotopic amplitude and latency maps (see Figure 6, "real" retinotopic maps). Subsequently, and in order to obtain the key features of these maps, the retinotopic distribution for each IC-ERP component was estimated by means of linear regression analysis (see Figure 6, "estimated" retinotopic

maps) (Smith and Kutas, 2015). Four regression analyses were carried out independently for each visual field quadrant, as previous analyses showed sharp transitions between them. For each regression analysis three predictor variables were used: the centroid position of the sector in the x-axis, the position in the y-axis and the interaction between them. As sectors were logarithmically spaced, we used the logarithms of the coordinates as predictor variables. Finally, as a measure of the goodness of fit, the correlation value between the real and the estimated retinotopic distributions of amplitude and latency was computed.

Visual field stimulation effects were statistically assessed by comparing mean amplitude and peak latency IC-ERP values in selected visual field regions. T-tests and repeated-measures analyses of variance (ANOVAs) were performed using a Greenhouse-Geisser correction for non-sphericity when required.

Source-Localization Analysis

This last analysis step aimed to assist in understanding the sensor-level retinotopic variations of the pattern-reversal ERP components. We employed beamforming (Gross et al., 2001; Van Veen et al., 1997) to estimate source-level ERPs generated by each voxel of a standard magnetic resonance image (MRI) in MNI (Montreal Neurological Institute) space. For this purpose, a standard boundary element method (BEM) volume conduction model (Oostenveld et al., 2003), as well as standard 10-10 electrode positions were employed. The MRI was segmented into a 10 mm resolution grid, and we computed the lead fields corresponding to the 3 possible orientations for each voxel. The single-trial covariance matrix for the entire time window of interest (from -100 to 400 ms) was calculated and employed to compute the spatial filter coefficients using linearly constrained minimum variance beamformer (LCMV; Van Veen et al., 1997).

Given the remarkable ERP differences between sectors observed in sensor-space, the spatial filter coefficients were computed separately for each sector. Regularization (lambda parameter) was set to 10%, i.e. a unit matrix scaled to 10% of the mean across eigenvalues of the covariance matrix was added to it. Then, each sensor-level trial was projected into each voxel of source-space through a spatial filter corresponding to a dipole located at that voxel with fixed optimal orientation. To avoid differences in amplitude due to voxels depth, source-level ERPs were all normalized as relative change with respect to the RMS of the baseline activity for each voxel (Capilla et al., 2013).

After estimating the source-level ERPs, we aimed to identify the brain regions underlying the previously characterized ERP components. To this end, we performed ICA on the source-level ERPs extracted for each sector and subject (i.e. 60 x 29 ERPs for each grid voxel) (see Figure 1 in Capilla et al., 2013 for a schematic explanation). It is important to mention that, as demonstrated by Jonmohamadi et al. (2014), source-space ICA is able to deal with multiple and correlated sources more efficiently than other source localization techniques, such as using only beamforming or dipole fitting on sensor-level ICs. Given the very high dimensionality of the data (> 1700 voxels), we performed a dimensionality reduction by principal component analysis (PCA) before applying ICA. The number of PCs was set to 4, as this was the number of components selected as meaningful in the sensor-level ICA and the choice that best matched the sensor-level ICs. Analyses restricting the data to 5, 6 or 7 dimensions yielded similar results, as shown in the Results section. The source-level ICs were matched with their corresponding sensor-level ICs by means of correlation analyses. As for the sensor-level ICs, each source-level IC waveform was normalized with respect to the RMS of its corresponding brain pattern. In this way, source-space IC units were converted to its

original unit, i.e. relative change with respect to baseline activity. Finally, the brain distribution of each source-level IC was obtained by rectifying the IC spatial distribution and smoothing it with a Gaussian kernel of 5 mm FWHM.

RESULTS

Behavioral Results

As expected performance in the secondary task was very high (hits 96.8 ± 2.9%, mean ± SD), demonstrating that participants were engaged in the experiment. Only one participant showed a significantly lower performance (82.3%, < 5 SD below the group mean), being excluded from the analyses for this reason.

Sensor-Level ERPs and Topographies

As shown in Figures 2-4, pattern-reversal stimulation elicited five ERP components: C1, P1, C2, N1 and P2 (sorted by latency). ERP waveforms were consistent across subjects when they were stimulated at different retinotopic positions as illustrated in Supplementary Figure 1. In the next paragraphs, we will briefly describe these ERP components.

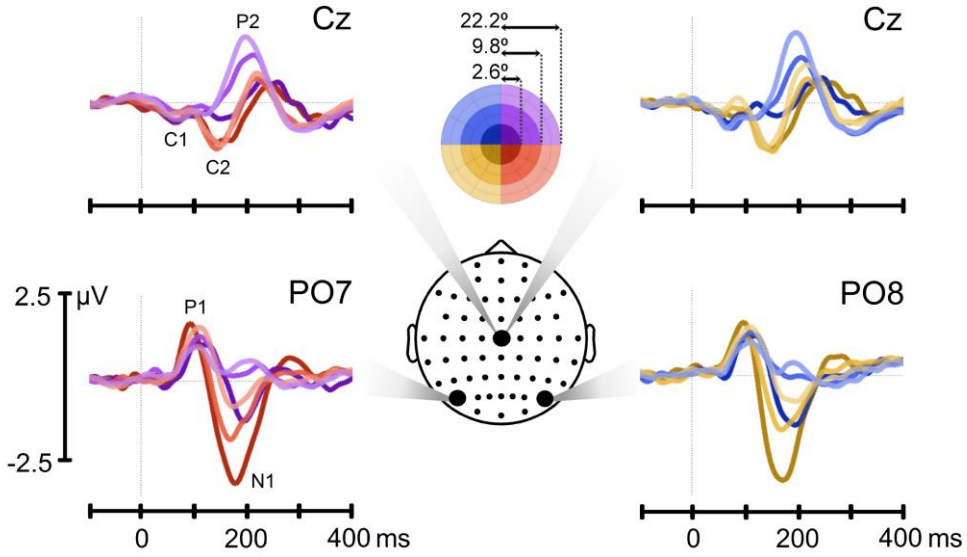

Figure 2. Sensor-level ERPs. Grand-average ERP waveforms elicited by pattern-reversal stimulation at 12 groups of sectors (4 quadrants coded by color, 3 eccentricities coded by color intensity). The left panels show the ERPs resulting from right hemifield stimulation, at Cz and contralateral site PO7. The right panels show the result of left visual field stimulation, at Cz and PO8. The five major ERP components found in this study are labeled.

C1 component was more clearly identifiable for upper field stimulation, where it showed a negative polarity peaking at about 70 ms over midline electrodes (Cz/CPz). The typical C1 polarity reversal was more evident for the most peripheral lower field sectors (see Figures 2 and 3).

The P1 component showed its maximal amplitude at contralateral parieto-occipital sites (PO7/PO8). On average it peaked at 105 ms, although there was some variability depending on the stimulated sector, as can be seen in Figure 2. The topographical distribution of P1 remained relatively stable across the visual field (Figure 4).

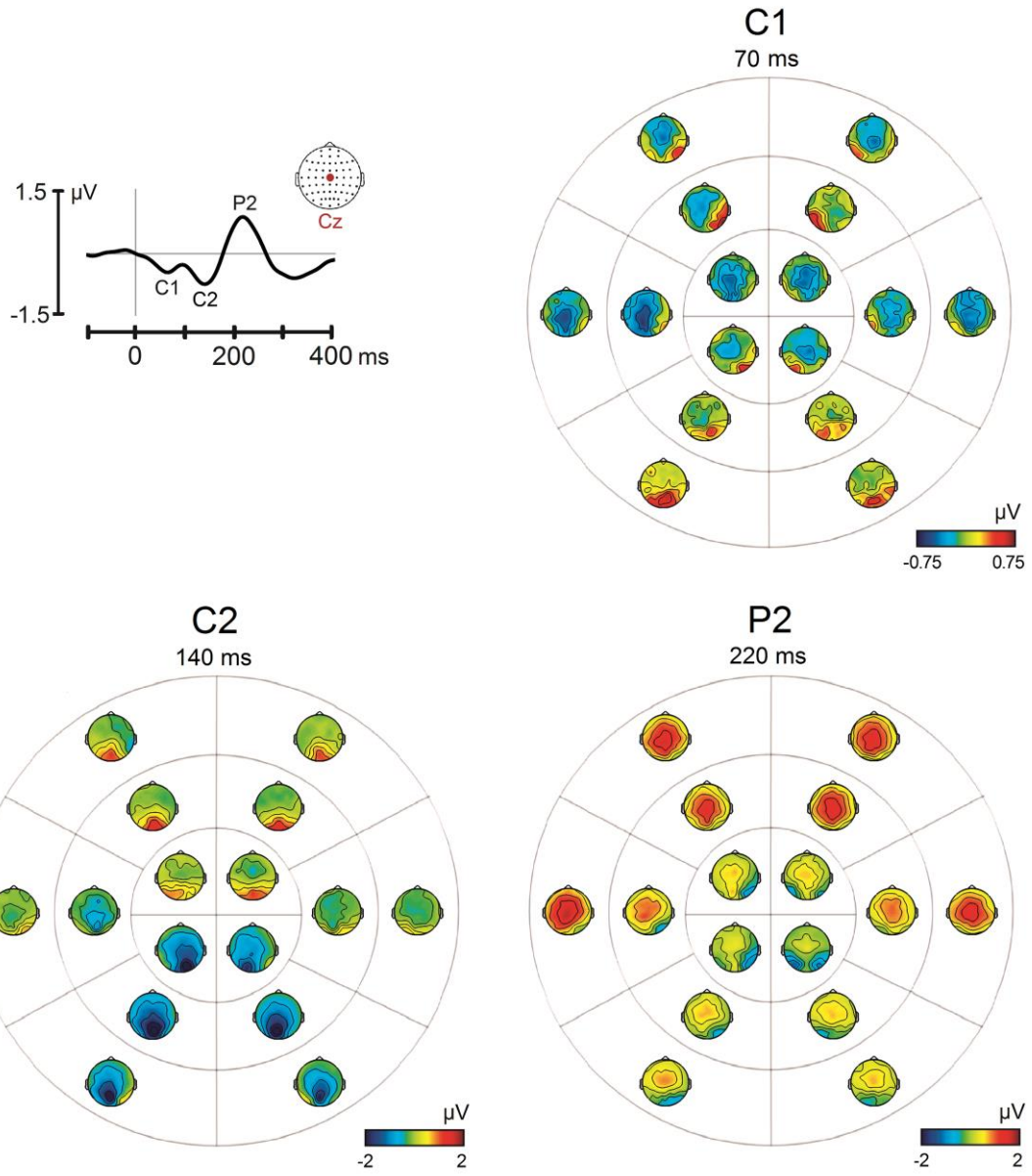

Figure 3. Sensor-level topographies of C1, C2 and P2 components. The uppermost left panel displays the grand-average ERP waveform at Cz, averaged across all sectors. The three ERP components, C1, C2 and P2 are indicated. The topographies of each component at the peak latency are shown in subsequent panels. Topographies are shown for a selection of 16 groups of visual field sectors.

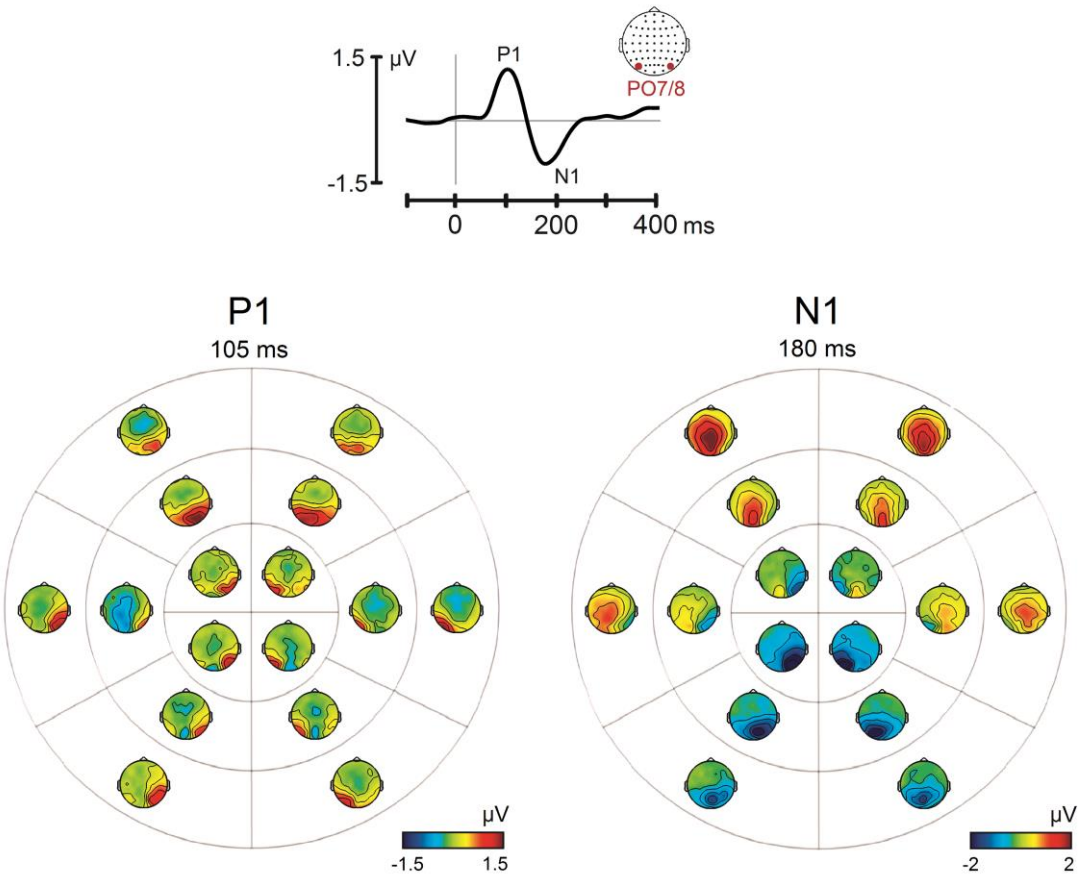

Figure 4. Sensor-level topographies of P1 and N1. The upper panel displays the grand-average ERP waveform at contralateral site PO7/8, averaged across all sectors. The topographies of P1 and N1 at their peak latencies are shown in the lower panels. Topographies are shown for a selection of 16 groups of visual field sectors.

The next component, peaking at about 140 ms, was distributed over midline parieto-occipital sites (POz). Although it was not evident at this stage, it was later confirmed by ICA that this component had a different polarity depending on the stimulated visual field; with positive polarity for upper field stimulation, and negative polarity for the lower visual field (Figure 3). Given its changing polarity, we will refer to it as C2.

As the P1 component, N1 showed the highest amplitude over parieto-occipital sites contralateral to stimulation (PO7/PO8). However, unlike P1, N1 component was virtually non-existent for upper visual field stimulation (Figures 2 and 4). The positive

polarity observed at this latency (~180 ms) for the peripheral upper visual field seems to be rather explained by the earlier onset of P2 in this region (see Figure 2). In addition, N1 was characterized by remarkable amplitude differences as a function of eccentricity, with the highest amplitudes evoked by foveal stimulation.

Finally, P2 component was characterized by a non-lateralized positive component peaking at about 220 ms over midline central sites (Cz). It was evident for the whole visual field, although it showed the highest amplitude, as well as the earliest latency, in response to peripheral upper visual field stimulation (Figures 2 and 3).

Independent Component (IC) Sensor-Level ERPs

As explained in the Methods section, ERP data was decomposed by ICA. The ERP activations and topographies of the resulting 59 ICs were visually inspected, and those that resembled the previously described ERP components at the sensor-level were selected. Four ICs were finally chosen (Figure 5). Two of them showed a midline topographical distribution, herein referred to as IC#1 and IC#4, whereas the other two ICs were strongly lateralized at left (IC#2) and right (IC#3) parieto-occipital sites. Taking together, they explained 51.3% of the variance. Individually, the percent variance accounted for by each of them was 5.3% for IC#1, 10.9% for IC#2, 10.8% for IC#3, and 24.9% for IC#4. Supplementary Figure 2 shows the ERPs resulting from back-projecting these four ICs, and illustrates how they retain the main features of the ERP components of interest (see Figure 2). As it can be observed in Figure 5, IC#1 captured C1 and C2; IC#2 and #3 accounted for the P1-N1 complex over contralateral left and right posterior sites respectively; and IC#4 mainly reflected the P2 component. The characteristic features of each component for each visual field quadrant (i.e. representative electrode, latency and polarity) are summarized in Table 1.

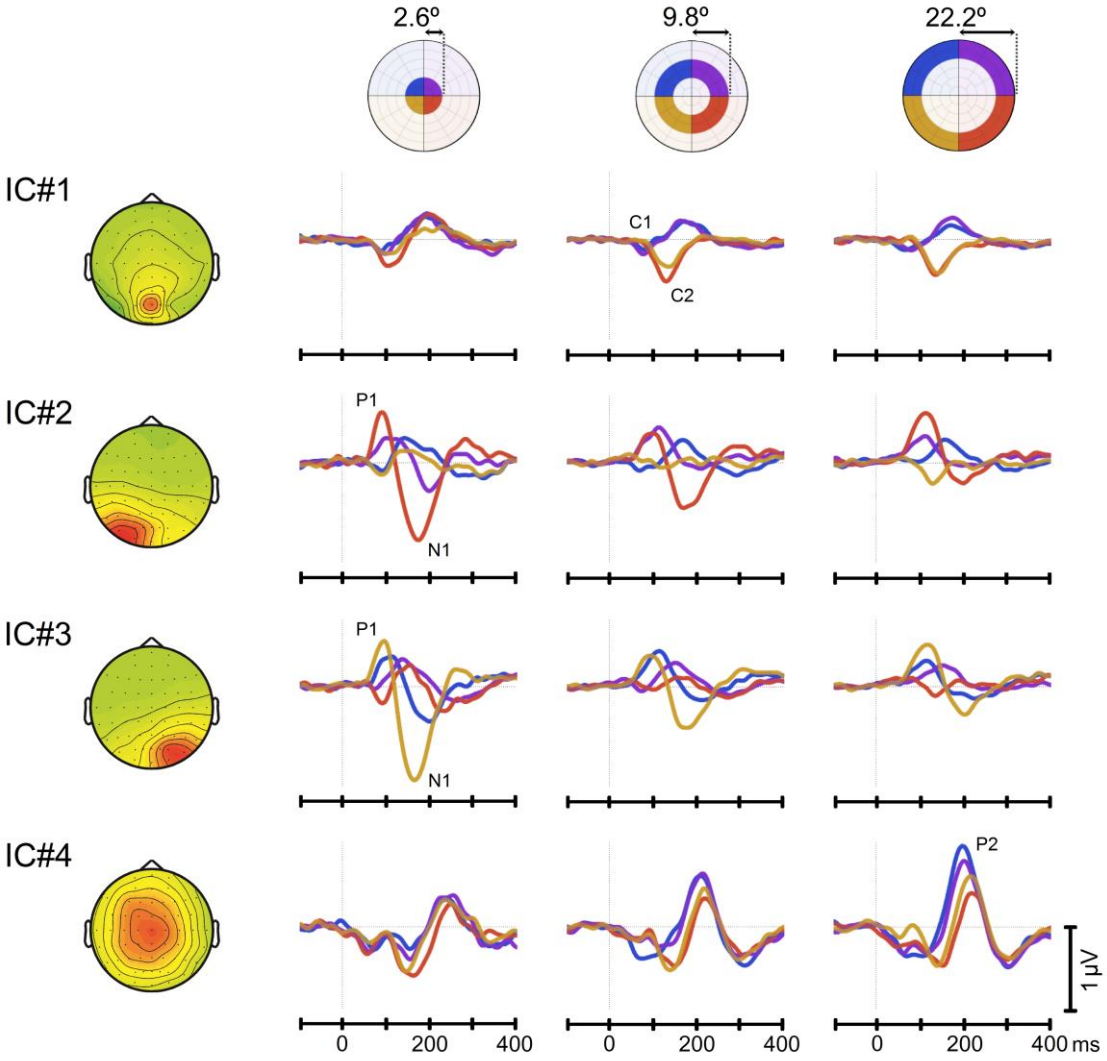

Figure 5. Independent component (IC) ERPs. The leftmost column shows the topography of each IC (IC#1 to IC#4; in arbitrary units, a.u.). Subsequent columns display the grand-average IC-ERP waveforms elicited by stimulation at different quadrants (color-coded) and eccentricity (foveal, perifoveal and peripheral regions, respectively).

	Upper field		Lower field	
	Right	Left	Right	Left
C1	POz - 82 ms	POz - 82 ms	POz + 63 ms	POz + 65 ms
P1	PO7 + 113 ms	PO8 + 113 ms	PO7 + 96 ms	PO8 + 99 ms
C2	POz + 184 ms	POz + 180 ms	POz - 130 ms	POz - 132 ms
N1	PO7 - 201 ms	PO8 - 203 ms	PO7 - 177 ms	PO8 - 175 ms
P2	Cz + 213 ms	Cz + 210 ms	Cz + 227 ms	Cz + 220 ms

Table 1. Electrode showing maximal amplitude, characteristic polarity (- for negative, + for positive), and peak latency for each IC-ERP component and visual field quadrant.

Retinotopic Distribution of Amplitude and Latency

Subsequently, retinotopic maps of amplitude and latency for each IC-ERP component were obtained. The results are shown in Figure 6. The figure shows the estimated retinotopic maps resulting from the regression analyses, the measured retinotopic distributions, and the correlation coefficient between them. In the case of the latency maps, the figure shows the difference between the latency at each sector and the average latency of the component. In the next subsections we will describe in detail these retinotopic distributions, as well as the statistical differences between different visual field regions (see Supplementary Figure 3). Additionally, the temporal evolution of each IC's amplitude can be found in video-clip format in the supplementary material (Supplementary Videos 1-4).

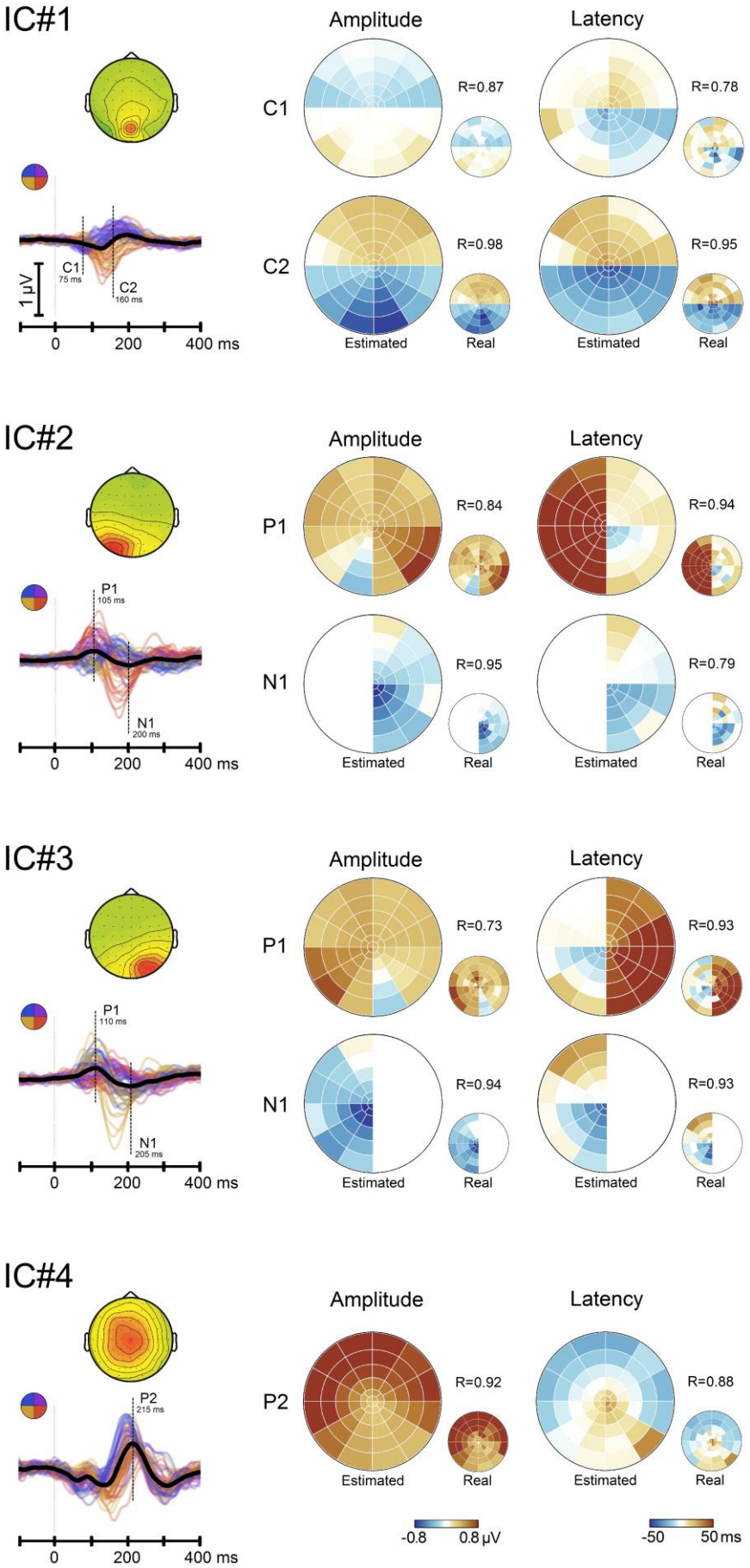
IC#1
Amplitude
Latency
C1
C2
R=0.87
R=0.78
R=0.98
R=0.95
C1
75 ms
C2
160 ms
1 µV
0
200
400 ms
Estimated
Real
IC#2
P1
N1
R=0.84
R=0.94
R=0.95
R=0.79
P1
105 ms
N1
200 ms
IC#3
R=0.73
R=0.93
R=0.94
R=0.93
P1
110 ms
N1
205 ms
IC#4
P2
R=0.92
R=0.88
P2
215 ms
-0.8
0.8 µV
-50
50 ms

Figure 6. Retinotopic maps. The figure shows the retinotopic distributions of amplitude (middle column) and latency (rightmost column) for each IC-ERP component. The leftmost column displays the topography of each IC and the ERP waveforms for all visual field sectors (color-coded by quadrant). The "real" retinotopic maps reproduce the measured amplitude and latency (difference with respect to the mean latency) for each IC-ERP component at each sector. The "estimated" retinotopic maps were obtained by means of regression analyses. The correlation coefficient between the real and estimated retinotopic maps are also indicated (R).

C1 component (IC#1)

The amplitude retinotopic map of C1 showed a negative polarity for the upper visual field (-0.28 ± 0.13 μV) that became positive for the lower field (0.14 ± 0.07 μV; t_{28} = 14.7, $p < .001$) (Supplementary Figure 3).

In addition, lower visual field stimulation elicited shorter C1 latencies compared to the upper hemifield (lower visual field: 63 ± 3 ms; upper visual field: 81 ± 3 ms; t_{28} = 20.3, $p < .001$) (see Supplementary Video 1).

C2 component (IC#1)

A critical result of this study was the finding that not only the C1 component but also the later and larger C2 component was characterized by a polarity inversion. As opposed to C1, the C2 component was positive for the upper visual field and negative for the lower field. Its amplitude, either negative or positive, was higher along the vertical meridian (negative C2: -0.67 ± 0.52 μV; positive C2: 0.45 ± 0.23 μV), compared to sectors closer to the horizontal meridian (negative C2: -0.37 ± 0.24 μV; positive C2: 0.29 ± 0.17 μV) (vertical Vs. horizontal meridian difference for negative C2: t_{28} = 4.8, for positive C2: t_{28} = 6.7; $p < .001$) (Supplementary Figure 3).

The negative and positive counterparts of the C2 component also showed strikingly different timing. On average, the negative C2 peaked in the lower field at 129 ± 3 ms,

whereas the latency of the positive C2 in the upper field was 177 ± 3 ms (t_{28} = 56.0, p < .001).

P1 component (IC#2 and #3)

The P1 component showed a similar behavior on left (IC#2) and right (IC#3) parieto-occipital sites and therefore, they will be described together (see Supplementary Videos 2 and 3). P1 amplitude was highest in the contralateral visual field, particularly at the peripheral region in the lower field immediately below the horizontal meridian, where it reached 0.85 ± 0.41 μV. The amplitude at this region was higher than at the fovea and perifovea (t_{28} = 2.1, p < .05), and also higher than at the contralateral upper field as a whole (t_{28} = 2.8, p < .01) (see Supplementary Figure 3).

Retinotopic mapping of latency showed a different distribution. Unlike the amplitude map, P1 latency showed a sharp transition across the vertical meridian, being its latency much shorter for contralateral (107 ± 3 ms) than for ipsilateral stimulation (163 ± 3 ms; t_{28} = 70.7, p < .001). Similar to P1 amplitude, the shortest latencies were observed over the contralateral lower quadrant. In this quadrant there was a clear eccentricity effect ($F_{2,56}$ = 106.9, p < .001), with shorter latencies for the foveal region (92 ± 8 ms) as compared to the perifovea (99 ± 5 ms) and the periphery (113 ± 5 ms) (lower t-value: t_{28} > 3.2, p < .004).

N1 component (IC#2 and #3)

N1 amplitude was also more pronounced for contralateral visual stimulation. Furthermore, N1 was not even evident for ipsilateral stimulation, so the retinotopic maps and the statistical results described here will be restricted to the contralateral visual field.

Similar to P1, N1 amplitude was highest for the lower hemifield, although in this case it was larger for the foveal region. N1 amplitude was modulated by eccentricity in the contralateral lower quadrant ($F_{2,56}$ = 22.0, p < .001): it was higher in the fovea (-1.21 ± 0.80 µV) compared to the perifovea (-0.71 ± 0.35 µV) and, in turn, higher than in the periphery (-0.46 ± 0.28 µV) (lower t-value: t_{28} > 3.9, p < .001) (Supplementary Figure 3).

A similar pattern was shown by the retinotopic distribution of N1 latency (eccentricity effect: $F_{2,56}$ = 125.5, p < .001). The contralateral N1 in the lower hemifield peaked at 169 ± 6 ms in the fovea. This was significantly earlier than in the perifovea (180 ± 6 ms) and, in turn, earlier than in the periphery (193 ± 6 ms) (t_{28} > 6.9, p < .001).

P2 component (IC#4)

Finally, P2 was a positive component elicited by stimuli presented throughout the whole visual field, although its amplitude was much more pronounced for stimulation at the periphery of the upper hemifield (Supplementary Video 4). In the upper visual field P2 amplitude exhibited an eccentricity effect ($F_{2,56}$ = 29.4, p < .001), with larger values in the periphery (1.08 ± 0.45 µV) than in the perifovea (0.87 ± 0.35 µV) and fovea (0.61 ± 0.29 µV) (lower t-value: t_{28} > 3.6, p < .002).

P2 latency exhibited a similar distribution. It was also characterized by an eccentricity effect in the upper hemifield ($F_{2,56}$ = 262.8, p < .001), where the periphery (197 ± 5 ms) elicited the shortest latency peaks. P2 peaked at 212 ± 4 ms for perifoveal stimulation and at 228 ± 6 ms when the foveal region was stimulated (t_{28} > 11.1, p < .001).

Brain Sources Underlying Visual ERP Components

The source-level ICs are shown in Figure 7. They were all highly correlated with their corresponding sensor-level ICs (0.66, 0.77, 0.81 and 0.85 for IC#1 to IC#4, respectively). The correlation values between non-corresponding source and sensor-level ICs were considerably lower, ranging from 0.01 to 0.33 (in absolute values). As previously mentioned, source-level ICs were obtained by applying an initial PCA decomposition into 4 PCs. Supplementary Figure 4 shows that reducing the data to more dimensions did not add further information.

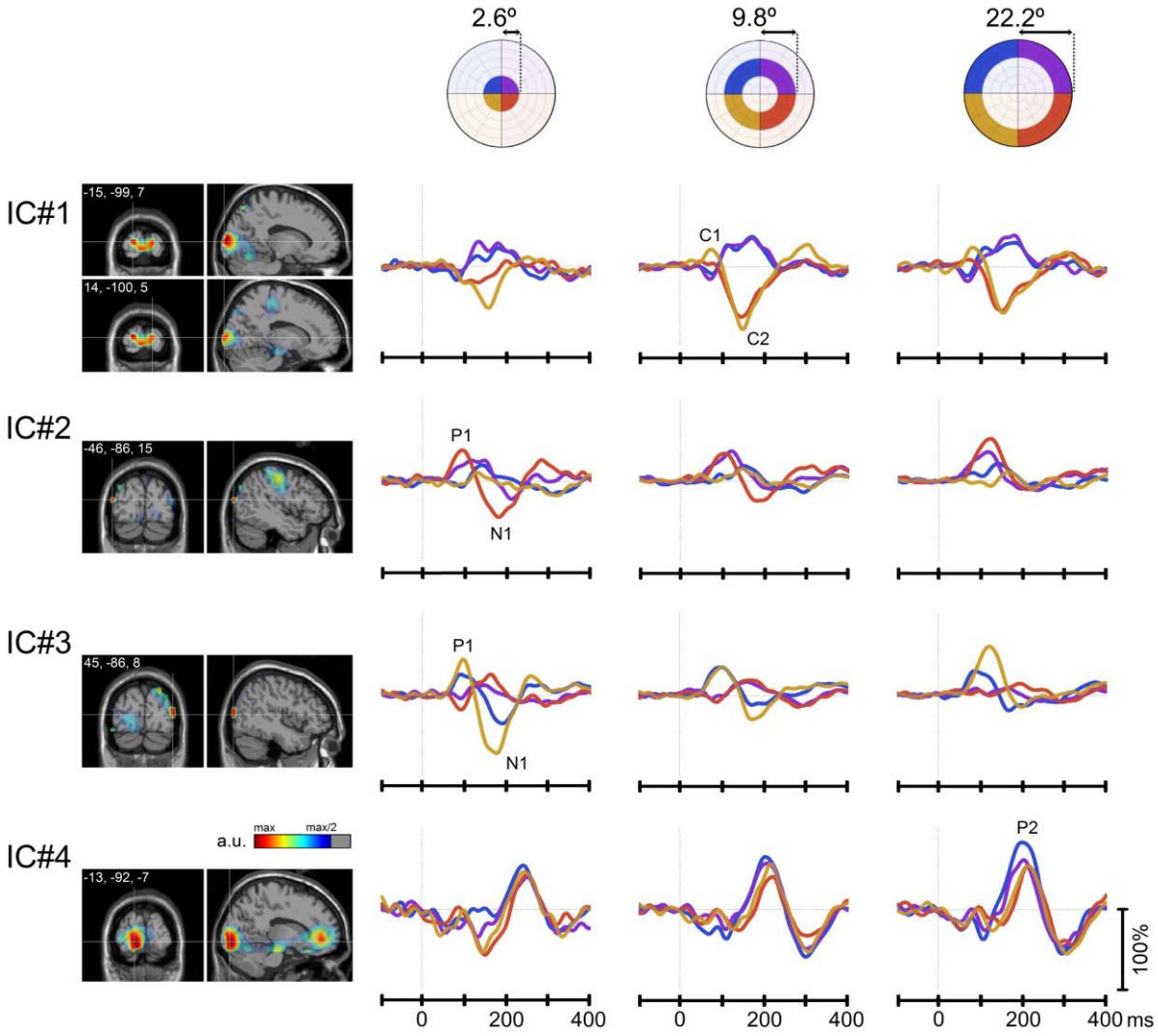

Figure 7. Brain sources underlying visual ERPs. The figure shows the results of applying ICA to the source-level ERPs. Source-level ICs have been sorted according to their corresponding sensor-level ICs (from IC#1 to IC#4). The leftmost column shows the brain pattern underlying each source-level IC (in arbitrary units, a.u.; MNI coordinates of the peak voxel are indicated). In analogy to figure 5, subsequent columns show the source-level waveforms for each quadrant (color-coded) and eccentricity (foveal, perifoveal and peripheral regions, respectively). These waveforms are normalized with respect to the RMS of the corresponding brain pattern and expressed as relative change with respect to baseline.

The MNI coordinates and underlying brain regions for each source-level IC are summarized in Table 2. The cortical sources accounting for IC#1 were located around the calcarine sulcus bilaterally (V1/V2). The underlying IC#4 generator was also confined to the striate cortex, over the left hemisphere and slightly deeper than IC#1 sources. It is important to note, however, that the beamforming results for IC#4 showed other strong local maxima over deep medial regions (see Figure 7) suggestive of a residuary center of the head bias, so the localization results for this IC should be taken cautiously. Finally, IC#2 and IC#3 were localized in the middle occipital gyrus of left and right hemisphere respectively, corresponding to dorsal extrastriate cortex.

	MNI Coordinates	Hemisphere	Brain Region
IC#1	[-15, -99, 7]	Left	Calcarine sulcus
	[14, -100, 5]	Right	Calcarine sulcus
IC#2	[-46, -86, 15]	Left	Dorsal extrastriate cortex
IC#3	[45, -86, 8]	Right	Dorsal extrastriate cortex
IC#4	[-13, -92, -7]	Left	Calcarine sulcus

Table 2. Source localization results: MNI coordinates and corresponding brain region underlying each source-level IC.

DISCUSSION

The present study provides an exhaustive retinotopic mapping of the pattern-reversal ERP. Inspired by previous mfVEP (Baseler and Sutter, 1997; Baseler et al., 1994; Fortune and Hood, 2003; Hood et al., 2003; Zhang and Hood, 2004) and ERP studies (Clark et al., 1995; Di Russo et al., 2002, 2005) our experimental design incorporated (i) extensive coverage of the visual field (around 45° of visual angle), (ii) a stimulation rate that minimizes neural adaptation (200-400 ms SOA), and (iii) multichannel scalp recordings of EEG responses (59 active electrodes). We made use of advanced analysis strategies, combining ICA and source localization techniques, in order to clarify the retinotopic differences observed at the scalp. It is worth mentioning that previous ERP studies have used electrodes below occipital sites (e.g. Iz) and ERP-dipole modeling in combination with functional MRI to estimate the cortical sources of visual ERP components (Di Russo et al., 2002, 2005). However, despite these differences, present source analysis results are in good agreement with those obtained by other methodological approaches.

Overall, our analyses revealed five major visual ERP components. Two of them, C1 and C2, showed inverted polarity for upper and lower visual fields. The P1-N1 complex had its highest amplitude and shortest latency when the lower contralateral quadrant was stimulated. Alternatively, P2 showed enhanced amplitudes and reduced latencies for peripheral upper field stimulation. In the following sections we shall describe in more detail the retinotopic organization of each ERP component, highlighting the optimal locations to boost each of them. In addition, we shall discuss how our findings may contribute to the current debate on the striate/extrastriate generators of the visual ERPs.

C1 component

The first component (C1) would correspond to the N75 elicited by conventional, large-field pattern reversal stimulation (Odom et al., 2004, 2010). As shown by many previous studies (Clark et al., 1995; Di Russo et al., 2002, 2005; Kelly et al., 2008, 2013b; Zhang and Hood, 2004) and replicated here, C1 polarity is largely dependent on stimulus position. This finding has been often presented as a proof that C1 arises from striate cortex (V1) (Clark et al., 1995; Di Russo et al., 2002; Tabuchi et al., 2002), as the voltage polarity observed at the scalp is consistent with the cruciform configuration of V1 (i.e. the upper and lower hemifields are respectively represented in the lower and upper banks of the calcarine sulcus; Jeffreys and Axford, 1972a, 1972b). However, it is important to bear in mind that a polarity inversion by itself does not constitute sufficient evidence of striate origin, since the retinotopic organization of extrastriate regions (V2/V3) could also lead to polarity inversions at the scalp (Ales et al., 2010b; for a recent discussion see Ales et al., 2013; Kelly et al., 2013a, 2013b).

Source localization analysis employed here showed that C1 originated around the calcarine fissure, in line with previous reports (Clark et al., 1995; Di Russo et al., 2002; Tabuchi et al., 2002). Moreover, our results are consistent not only with the polarity inversion criteria but also with additional predictions derived from the cruciform model, pointing to a striate origin of C1 (Kelly et al., 2013b). First, assuming a surface-negative activation, the predicted polarity would be negative for the upper hemifield and positive for the lower, as shown in Figure 6 and in consonance with previous research findings (Clark et al., 1995; Di Russo et al., 2002, 2005; Kelly et al., 2013b). Second, it has been posited that if the lower bank of the calcarine sulcus is not perfectly oriented in the horizontal, it would tend to point to the medial plane, and would thus be captured by ipsilateral electrodes (Kelly et al., 2013b). This would lead to asymmetry in the

topographies for upper and lower stimulation, being slightly ipsilateral for the upper and contralateral for the lower hemifield. Our C1 scalp topographies (Figure 3), similar to those shown in previous studies (Di Russo et al., 2002, 2005; Kelly et al., 2013b), are consistent with this prediction. Finally, the retinotopic map of C1 amplitude suggests that the polarity reversal point of C1 is not located at exactly the horizontal meridian, but rather in the 0°-30° range in the lower hemifield (see Figure 6). This is in agreement with Clark and colleagues (1995), who found that the reversal point was on average 15°-20° below the horizontal meridian. Subsequent studies have replicated this finding (Aine et al., 1996; Kelly et al., 2013b; Zhang and Hood, 2004) suggesting that the optimal locations for boosting the C1 inversion effect are not symmetrical (around 25° above and 45° below the horizontal meridian) (Di Russo et al., 2002, 2005, 2008, 2012). This finding implies that the horizontal meridian might not be represented at the apex of the calcarine sulcus, but rather in the lower bank (Clark et al., 1995), though this has not yet been conclusively demonstrated (Ales et al., 2013). Nevertheless, the smooth transition observed for C1 across the horizontal meridian seems more compatible with a striate source, given that the ventral and dorsal segments of extrastriate regions V2 and V3 are precisely divided by the horizontal meridian (Horton and Hoyt, 1991a; Sereno et al., 1995). Taken together, therefore, present results support the notion that V1 is the dominant generator of the C1 component.

C2 component

In a similar way to C1, the subsequent C2 component also inverted its polarity for upper and lower hemifields (i.e. positive for upper and negative for lower field stimulation). This component was not evident in the initial sensor-level ERPs, but rather emerged when ERPs were unraveled by ICA. In the raw ERPs, C2 was negative (see Figure 2),

probably as the result of the superposition between C2 and the N1 component peaking in the same time window (130-200 ms). In the upper hemifield, the opposite polarities of the positive C2 and N1 might have resulted in cancelation, whereas in the lower hemifield, both C2 and N1 were negative, resulting in a prominent negative component (see Figure 2; Di Russo et al., 2005). It is possible that C2 went largely unnoticed in previous research for this reason. An exception is the studies carried out by Di Russo and colleagues (Di Russo et al., 2005, 2012) which described a similar component, called C2 or P125/N135 (for upper and lower hemifield respectively) and originating from the same brain source as C1.

Present source-space ICA analyses revealed that both C1 and C2 originated around the calcarine fissure. However, unlike the case of the retinotopic distribution of C1 amplitude, C2 exhibited its highest amplitude along the vertical meridian. This suggests that C2 arises from the confluence of V1 and V2, where the vertical meridian is represented (Sereno et al., 1995; Wandell et al., 2007). Furthermore, it could be hypothesized that C2 is mostly generated in V2 rather than V1, given that (i) the waveform and timing of the C2 component closely parallels the one predicted for V2 (Ales et al., 2010a) and (ii) as mentioned above, the sharp transition of C2 amplitude between the upper and lower hemifields is suggestive of origin in extrastriate cortex, whose representation of the visual field above and below the horizontal meridian is segregated in ventral and dorsal sections (Horton and Hoyt, 1991a; Sereno et al., 1995; Wandell et al., 2007).

However, although the retinotopic features of C1 and C2 suggest generators located in V1 and V2 respectively, the latency difference between the two components is greater than the expected delay between V1 and V2 (Ales et al., 2010a, Hagler et al., 2009). This discrepancy might be explained by the fact that the methodological approach used

here was not able to disambiguate the responses from these two adjacent visual areas (unlike the approach employed by Ales et al., 2010a or Hagler et al., 2009). In this way, the waveform of IC#1 could be the result of the summed V1 and V2 responses. If, as shown by the two above-mentioned studies, the response amplitude is higher for V1 compared to V2 during the first time window, the summed response would be initially dominated by V1 features. If, later on, V2 amplitude is higher, the features of this area will predominate in the summed response. For example, as it can be seen in Supplementary Video 1, some retinotopic features indicative of a V2 origin (e.g. strongest amplitude along the vertical meridian) are already present at 105-110 ms, before the C2 component peaks.

P1-N1 complex

Unlike the rest of midline components, P1 and N1 appeared as strongly lateralized, with maximum activity over parieto-occipital electrodes contralateral to stimulation. On average P1 peaked at about 100 ms and N1 at about 180 ms, though their latencies were highly dependent on stimulus location. The retinotopic distribution of latency was very similar in the two cases, showing earlier activity for stimulation at foveal locations in the contralateral lower quadrant. In general, amplitude was also maximal when stimuli were presented in the contralateral lower quadrant, though the retinotopic distribution of amplitude showed some differences between the two components, as described below.

On the one hand, and in line with previous reports (Clark et al., 1995; Di Russo et al., 2002, 2005), P1 amplitude was not very sensitive to stimulus location. Although it was higher for the contralateral lower quadrant, especially at peripheral locations, P1 was also evident for the contralateral upper field and even for the ipsilateral hemifield (though at significantly longer latencies and exhibiting a negative polarity in some

sectors, see Figure 6). On the other hand, N1 was much more sensitive to stimulus location. Like P1, it showed maximal amplitude for the contralateral lower quadrant, although preferentially at central locations. However, unlike P1, the N1 component was markedly reduced for the upper visual field and non-detectable for ipsilateral stimulation.

Despite the above-mentioned differences in retinotopic distribution, the two components were captured by a single IC at both sensor and source-level (IC#2 for left hemisphere activity and IC#3 for right hemisphere). This suggests that P1 and N1 components are generated by an activation of nearby regions, in line with previous reports (Clark et al., 1995; Di Russo et al., 2002; Novitskiy et al., 2011). For this reason we have grouped them as the P1-N1 complex. As was the case for the C2 component, the retinotopic map of the P1-N1 complex showed a striking transition at the horizontal meridian, suggestive of extrastriate sources. In addition, the observed amplitude enhancement elicited by stimulation in the lower field would indicate a dorsal generator. This would be in agreement with previous studies (Clark et al., 1995; Di Russo et al., 2002; Martinez et al., 1999; Novitskiy et al., 2011), as well as with our beamforming results, which located the main generator of the P1-N1 complex around the dorsal part of extrastriate area V3. Moreover, the characteristic topography and biphasic waveform of the P1-N1 complex largely resemble the estimated activity of this brain region (Ales et al., 2010b; Hagler et al., 2009).

It is possible that the ventral part of V3 representing the upper visual field (i.e. VP; Burkhalter et al., 1986; Sereno et al., 1995) contributed to the P1-N1 complex, but with lower intensity. This lower intensity might be simply explained by the distance from the source to the electrodes, which would be shorter for area V3 compared to VP. However, some evidence suggests a real advantage for the lower hemifield, both in the strength of

electrophysiological (Portin et al., 1999) and behavioral (Carrasco et al., 2001; Levine and McAnany, 2005; Liu et al., 2006) responses. This functional benefit might be explained by the anatomical overrepresentation of the lower hemifield in the retina (Perry and Cowey, 1985), the lateral geniculate nucleus (Connolly and Van Essen, 1984) and V1 (Van Essen et al., 1984). Furthermore, dorsal V3, unlike its ventral counterpart, has reciprocal connections with V1 and is more myelinated (Burkhalter et al., 1986). Overall, these anatomical and functional asymmetries might explain the higher amplitude and shorter latencies observed for the P1-N1 complex in the lower visual field.

P2 component

Finally, we observed a positive component at about 220 ms. As in previous research, the P2 component showed a mid-central scalp distribution and was more prominent for upper field stimulation (Di Russo et al., 2002, 2008; but see Clark et al., 1995, for a larger P2 with lower field stimulation). We also found that P2 had increasingly higher amplitudes and shorter latencies as stimuli were more peripherally presented (especially for eccentricities above 10°; see Figure 6).

As previously mentioned, the results of P2 generation should be interpreted with caution given the presence of activation foci over deep medial areas. Nevertheless, our source localization analysis identified one occipital generator of P2 around the calcarine fissure (V1/V2), similar to the location of C1 and C2 sources, though slightly deeper. This would fit with the larger P2 for stimuli appearing at the periphery, as this is more anteriorly represented in visual cortex than the fovea (Wandell et al., 2007). It has been previously proposed that P2 might be a sign of V1 reactivation, due to top-down feedback from higher level visual areas back to primary visual cortex (Di Russo et al.,

2008). This could explain why P2 is not clearly seen with the mfVEP technique (e.g. Zhang and Hood, 2004), as the rapid stimulation rates employed in these studies might have prevented feedback to V1.

The smooth retinotopic distribution of P2 (see Figure 6) would support the notion that this component arises from striate cortex. However, in conflict with this hypothesis, P2 polarity was positive for the whole visual field, while a V1 source would be expected to produce a polarity inversion between upper and lower hemifields. The absence of a polarity inversion in this case might be explained by the anatomy of the calcarine sulcus. Based on Horton and Hoyt's (1991b) map of the representation of the visual field in V1, we speculate that the curvature of the upper calcarine bank representing peripheral locations from 10° to 20° (the eccentricity range with a larger P2) might result in signal cancelation at the scalp. In contrast, the lower bank of the calcarine would not be subjected to this opposing geometry, resulting in clear responses when the upper visual field is stimulated. This interpretation is nevertheless tentative, as V1 anatomy and folding patterns are highly variable among individuals (Stensaas et al., 1974), and we do not have access to the individual MRIs that could confirm it.

CONCLUSIONS

In conclusion, present results demonstrate that visual ERPs are considerably affected by stimulus location. Furthermore, we have quantified such an effect, providing the first systematic retinotopic mapping of amplitude and latency of major visual ERP components. These findings could be applied in future ERP studies to select optimal spatial locations for visual stimulation.

ACKNOWLEDGEMENTS: This work was supported by the Spanish Ministry of Science and Innovation/Economy and Competitiveness (MICINN/MINECO) (PSI2011-26314, PSI2012-34558 and PSI2014-54853-P).

REFERENCES

Aine, C.J., Supek, S., George, J.S., Ranken, D., Lewine, J., Sanders, J., Best, E., Tiee, W., Flynn, E.R., Wood, C.C., 1996. Retinotopic organization of human visual cortex: departures from the classical model. Cereb Cortex 6, 354-361.

Ales, J., Carney, T., Klein, S.A., 2010a. The folding fingerprint of visual cortex reveals the timing of human V1 and V2. Neuroimage 49, 2494-2502.

Ales, J.M., Yates, J.L., Norcia, A.M., 2010b. V1 is not uniquely identified by polarity reversals of responses to upper and lower visual field stimuli. Neuroimage 52, 1401-1409.

Ales, J.M., Yates, J.L., Norcia, A.M., 2013. On determining the intracranial sources of visual evoked potentials from scalp topography: a reply to Kelly et al. (this issue). Neuroimage 64, 703-711.

Baseler, H. A., Sutter, E. E., 1997. M and P components of the VEP and their visual field distribution. Vision Res 37: 675–690

Baseler, H.A., Sutter, E.E., Klein, S.A., Carney, T., 1994. The topography of visual evoked response properties across the visual field. Electroencephalogr Clin Neurophysiol 90, 65-81.

Bell, A.J., Sejnowski, T.J., 1995. An information-maximization approach to blind separation and blind deconvolution. Neural Comput 7, 1129-1159.

Brainard, D.H., 1997. The Psychophysics Toolbox. Spat Vis 10, 433-436.

Burkhalter, A., Felleman, D.J., Newsome, W.T., Van Essen, D.C., 1986. Anatomical and physiological asymmetries related to visual areas V3 and VP in macaque extrastriate cortex. Vision Res 26, 63-80.

Capilla, A., Belin, P., Gross, J., 2013. The early spatio-temporal correlates and task independence of cerebral voice processing studied with MEG. Cereb Cortex 23, 1388-1395.

Capilla, A., Pazo-Álvarez, P., Darriba, A., Campo, P., Gross, J., 2011. Steady-state visual evoked potentials can be explained by temporal superposition of transient event-related responses. PLoS One 6(1): e14543.

Carrasco, M., Talgar, C.P., Cameron, E.L., 2001. Characterizing visual performance fields: effects of transient covert attention, spatial frequency, eccentricity, task and set size. Spat Vis 15, 61-75.

Clark, V.P., Fan, S., Hillyard, S.A., 1995. Identification of early visual evoked potential generators by retinotopic and topographic analyses. Hum Brain Mapp 2, 170-187.

Connolly, M., Van Essen, D., 1984. The representation of the visual field in parvocellular and magnocellular layers of the lateral geniculate nucleus in the macaque monkey. J Comp Neurol 226, 544-564.

Di Russo, F., Aprile, T., Spitoni, G., Spinelli, D., 2008. Impaired visual processing of contralesional stimuli in neglect patients: a visual-evoked potential study. Brain 131, 842-854.

Di Russo, F., Martinez, A., Sereno, M.I., Pitzalis, S., Hillyard, S.A., 2002. Cortical sources of the early components of the visual evoked potential. Hum Brain Mapp 15, 95-111.

Di Russo, F., Pitzalis, S., Spitoni, G., Aprile, T., Patria, F., Spinelli, D., Hillyard, S.A., 2005. Identification of the neural sources of the pattern-reversal VEP. Neuroimage 24, 874-886.

Di Russo, F., Stella, A., Spitoni, G., Strappini, F., Sdoia, S., Galati, G., Hillyard, S.A., Spinelli, D., Pitzalis, S., 2012. Spatiotemporal brain mapping of spatial attention effects on pattern-reversal ERPs. Hum Brain Mapp 33, 1334-1351.

Fortune, B., Hood, D.C., 2003. Conventional pattern-reversal VEPs are not equivalent to summed multifocal VEPs. Invest Ophthalmol Vis Sci 44, 1364-1375.

Gross, J., Kujala, J., Hamalainen, M., Timmermann, L., Schnitzler, A., Salmelin, R., 2001. Dynamic imaging of coherent sources: Studying neural interactions in the human brain. Proc Natl Acad Sci U S A 98, 694-699.

Hagler, D.J., Jr., Halgren, E., Martinez, A., Huang, M., Hillyard, S.A., Dale, A.M., 2009. Source estimates for MEG/EEG visual evoked responses constrained by multiple, retinotopically-mapped stimulus locations. Hum Brain Mapp 30, 1290-1309.

Hood, D.C., Odel, J.G., Winn, B.J., 2003. The multifocal visual evoked potential. J Neuroophthalmol 23, 279-289.

Horton, J.C., Hoyt, W.F., 1991a. Quadrantic visual field defects. A hallmark of lesions in extrastriate (V2/V3) cortex. Brain 114 (Pt 4), 1703-1718.

Horton, J.C., Hoyt, W.F., 1991b. The representation of the visual field in human striate cortex. A revision of the classic Holmes map. Arch Ophthalmol 109, 816-824.

Jeffreys, D.A., Axford, J.G., 1972a. Source locations of pattern-specific components of human visual evoked potentials. I. Component of striate cortical origin. Exp Brain Res 16, 1-21.

Jeffreys, D.A., Axford, J.G., 1972b. Source locations of pattern-specific components of human visual evoked potentials. II. Component of extrastriate cortical origin. Exp Brain Res 16, 22-40.

Jonmohamadi, Y., Poudel, G., Innes, C., Jones, R., 2014. Source-space ICA for EEG source separation, localization, and time-course reconstruction. Neuroimage 101, 720-737.

Kelly, S.P., Gomez-Ramirez, M., Foxe, J.J., 2008. Spatial attention modulates initial afferent activity in human primary visual cortex. Cereb Cortex 18, 2629-2636.

Kelly, S.P., Schroeder, C.E., Lalor, E.C., 2013a. What does polarity inversion of extrastriate activity tell us about striate contributions to the early VEP? A comment on Ales et al. (2010). Neuroimage 76, 442-445.

Kelly, S.P., Vanegas, M.I., Schroeder, C.E., Lalor, E.C., 2013b. The cruciform model of striate generation of the early VEP, re-illustrated, not revoked: a reply to Ales et al. (2013). Neuroimage 82, 154-159.

Key, A.P., Dove, G.O., Maguire, M.J., 2005. Linking brainwaves to the brain: an ERP primer. Dev Neuropsychol 27, 183-215.

Klimesch, W., 2011. Evoked alpha and early access to the knowledge system: the P1 inhibition timing hypothesis. Brain Res 1408, 52-71.

Lee, T.W., Girolami, M., Sejnowski, T.J., 1999. Independent component analysis using an extended infomax algorithm for mixed subgaussian and supergaussian sources. Neural Comput 11, 417-441.

Levine, M.W., McAnany, J.J., 2005. The relative capabilities of the upper and lower visual hemifields. Vision Res 45, 2820-2830.

Liu, T., Heeger, D.J., Carrasco, M., 2006. Neural correlates of the visual vertical meridian asymmetry. J Vis 6, 1294-1306.

Makeig, S., Bell, A.J., Jung, T.P., Sejnowski, T.J., 1996. Independent component analysis of electroencephalographic data. In: Touretzky, D., Mozer, M., Hasselmo, M. (Eds.), Advances in Neural Information Processing Systems. MIT Press, Cambridge MA, pp. 145-151.

Mangun, G.R., Buonocore, M.H., Girelli, M., Jha, A.P., 1998. ERP and fMRI measures of visual spatial selective attention. Hum Brain Mapp 6, 383-389.

Martinez, A., Anllo-Vento, L., Sereno, M.I., Frank, L.R., Buxton, R.B., Dubowitz, D.J., Wong, E.C., Hinrichs, H., Heinze, H.J., Hillyard, S.A., 1999. Involvement of striate and extrastriate visual cortical areas in spatial attention. Nat Neurosci 2, 364-369.

Novitskiy, N., Ramautar, J.R., Vanderperren, K., De Vos, M., Mennes, M., Mijovic, B., Vanrumste, B., Stiers, P., Van den Bergh, B., Lagae, L., Sunaert, S., Van Huffel, S., Wagemans, J., 2011. The BOLD correlates of the visual P1 and N1 in single-trial analysis of simultaneous EEG-fMRI recordings during a spatial detection task. Neuroimage 54, 824-385.

Nunez, P., 1981. Electric Fields of the Brain: The Neurophysics of EEG, 1st ed. Oxford University Press, New York.

Nunez, P., Srinivasan, R., 2006. Electric Fields of the Brain: The Neurophysics of EEG, 2nd ed., 2nd ed. Oxford University Press, New York.

Odom, J.V., Bach, M., Barber, C., Brigell, M., Marmor, M.F., Tormene, A.P., Holder, G.E., Vaegan, 2004. Visual evoked potentials standard (2004). Doc Ophthalmol 108, 115-123.

Odom, J.V., Bach, M., Brigell, M., Holder, G.E., McCulloch, D.L., Tormene, A.P., Vaegan, 2010. ISCEV standard for clinical visual evoked potentials (2009 update). Doc Ophthalmol 120, 111-119.

Onton, J., Makeig, S., 2006. Information-based modeling of event-related brain dynamics. Prog Brain Res 159, 99-120.

Oostenveld, R., Fries, P., Maris, E., Schoffelen, J.M., 2011. FieldTrip: Open source software for advanced analysis of MEG, EEG, and invasive electrophysiological data. Comput Intell Neurosci 2011, 156869.

Oostenveld, R., Stegeman, D.F., Praamstra, P., van Oosterom, A., 2003. Brain symmetry and topographic analysis of lateralized event-related potentials. Clin Neurophysiol 114, 1194-1202.

Perry, V.H., Cowey, A., 1985. The ganglion cell and cone distributions in the monkey's retina: implications for central magnification factors. Vision Res 25, 1795-1810.

Portin, K., Vanni, S., Virsu, V., Hari, R., 1999. Stronger occipital cortical activation to lower than upper visual field stimuli. Neuromagnetic recordings. Exp Brain Res 124, 287-294.

Sereno, M.I., Dale, A.M., Reppas, J.B., Kwong, K.K., Belliveau, J.W., Brady, T.J., Rosen, B.R., Tootell, R.B., 1995. Borders of multiple visual areas in humans revealed by functional magnetic resonance imaging. Science 268, 889-893.

Smith, N.J., Kutas, M., 2015. Regression-based estimation of ERP waveforms: I. The rERP framework. Psychophysiology 52, 157-168.

Stensaas, S.S., Eddington, D.K., Dobelle, W.H., 1974. The topography and variability of the primary visual cortex in man. J Neurosurg 40, 747-755.

Sutter, E.E., 2001. Imaging visual function with the multifocal m-sequence technique. Vision Res 41, 1241-1255.

Tabuchi, H., Yokoyama, T., Shimogawara, M., Shiraki, K., Nagasaka, E., Miki, T., 2002. Study of the visual evoked magnetic field with the m-sequence technique. Invest Ophthalmol Vis Sci 43, 2045-2054.

Van Essen, D.C., Newsome, W.T., Maunsell, J.H., 1984. The visual field representation in striate cortex of the macaque monkey: asymmetries, anisotropies, and individual variability. Vision Res 24, 429-448.

Van Veen, B.D., Van Drongelen, W., Yuchtman, M., Suzuki, A., 1997. Localization of brain electrical activity via linearly constrained minimum variance spatial filtering. IEEE Trans Biomed Eng 44, 867-880.

Verleger, R., 1993. Valid identification of blink artefacts: are they larger than 50 microV in EEG records? Electroencephalogr Clin Neurophysiol 87, 354-363.

Wandell, B.A., Dumoulin, S.O., Brewer, A.A., 2007. Visual field maps in human cortex. Neuron 56, 366-383.

Wu, J., Yan, T., Zhang, Z., Jin, F., Guo, Q., 2012. Retinotopic mapping of the peripheral visual field to human visual cortex by functional magnetic resonance imaging. Hum Brain Mapp 33, 1727-1740.

Zerouali, Y., Lina, J.M., Jemel, B., 2013. Optimal eye-gaze fixation position for face-related neural responses. PLoS One 8, e60128.

Zhang, X., Hood, D.C., 2004. A principal component analysis of multifocal pattern reversal VEP. J Vis 4, 32-43.